Octahedral Pt-MOF with Au deposition for plasmonic effect and Schottky junction enhanced hydrogenothermal therapy of rheumatoid arthritis

Wenzhen Pan [a],[1], Zheng Li [a],[1], Shang Qiu [a],[1], Chengbai Dai [a], Shengyue Wu [a], Xin Zheng [a], Ming Guan [b],[**], Fenglei Gao [a],[*]

[a] *Jiangsu Key Laboratory of New Drug Research and Clinical Pharmacy, Xuzhou Medical University, Xuzhou, Jiangsu, 221002, China*
[b] *Department of Laboratory Medicine, Huashan Hospital, Shanghai Medical College, Fudan University, Shanghai, 200040, China*

ABSTRACT

Hydrogen (H_2) therapy is a novel and rapidly developing strategy utilized to treat inflammatory diseases. However, the therapeutic efficacy of H_2 is largely limited with on-target off-synovium toxic effect, nonpolarity and low solubility. Herein, an intelligent H_2 nanogenerator based upon the metal-organic framework (MOF) loaded with polydopamine and Perovskite quantum dots is constructed for the actualization of hydrogenothermal therapy. The biodegradable polydopamine with excellent photothermal conversion efficiencies is used for photothermal therapy (PTT) of rheumatoid arthritis (RA) and perovskite quantum dots (QDs) with unique photophysical properties are used as fluorescent signals for positioning Pt-MOF@Au@QDs/PDA nanoparticles. In addition, the Pt-MOF@Au@QDs/PDA catalyzer combines Au's surface plasmon resonance excitation with Pt-MOF Schottky junction, and exhibits extremely efficient photocatalytic H_2 production under visible light irradiation. The Pt-MOF@Au@QDs/PDA achieves the aggregation of rheumatoid synovial cells by the extravasation through "ELVIS" effect (extravasation through leaky vasculature and subsequent inflammatory cell-mediated sequestration) and extremely efficient photocatalytic H_2 production. By combining PTT and H_2 therapy, the Pt-MOF@Au@QDs/PDA relieves the oxidative stress of RA, and shows significant improvement in joint damage and inhibition of the overall arthritis severity of collagen-induced RA mouse models. Therefore, the Pt-MOF@Au@QDs/PDA shows great potential in the treatment of RA and further clinical transformation.

1. Introduction

Rheumatoid arthritis (RA) is a chronic autoimmune systemic inflammatory disease characterized by synovial hyperplasia and recruitment of inflammatory cells, ultimately leading to bone destruction, joint deformities, and eventually disability [1–4]. Although the etiology of RA is still controversial, its pathological process is comparatively distinct. The massive recruitment and infiltration of inflammatory cells promotes synovial hyperplasia, leading to the overexpression of class II major histocompatibility complex antigens [5–8]. Generation of a series of degradative enzymes and acute oxidative stress induced by inflammation cause severe bone and cartilage damage of rheumatoid joints. Therefore, removal of proliferating synovial fibroblasts and buffering oxidative stress in local joints is an effective way to treat RA.

As an anti-oxidative stress agent, hydrogen (H_2) has shown great potential in the prevention and treatment of oxidative stress [9,10]. H_2 can rapidly diffuse across membranes and reduce harmful reactive oxygen species (ROS) in cells, especially hydroxyl radicals (·OH), which can protect cells. Although they are cytotoxic, low concentrations of O_2^- and H_2O_2 play a very important role in maintaining normal physiological functions such as cell proliferation and apoptosis. Thus, it is essential to neutralize cytotoxic ROS without affecting the basic biological activities of other ROS [11,12]. Shigeo et al. demonstrated that H_2 can reduce cytotoxicity caused by ·OH without compromising other ROS, and proposed that H_2 as an antioxidant has the potential to prevent and treat diseases [13]. Furthermore, previous studies have shown that the combination of gas therapy with conventional treatment has synergetic therapeutic effects [14–18]. He et al. indicated that hydrogenothermal therapy can not only synergistically enhance the anti-tumor effect, but also has the potential to protect normal tissue cells from hyperthermia
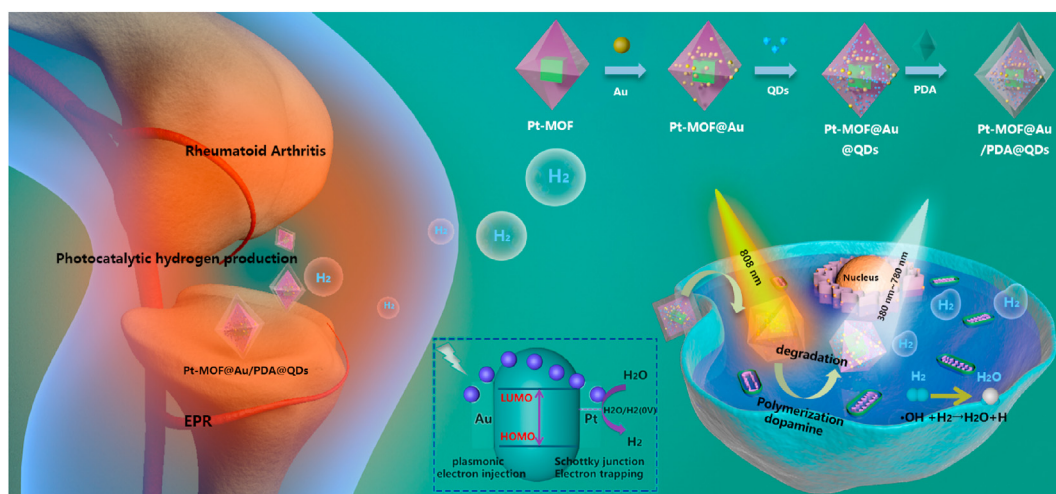
Scheme 1. Schematic illustration of the synthesis route and the hydrogen-photothermal treatment therapeutic mechanism based on the Pt-MOF@Au@QDs/PDA; (I) reasonable design and synthesis procedures of Pt-MOF@Au@QDs/PDA nanoregulator; (II) the enhanced permeation and retention effect enables the Pt-MOF@Au@QDs/PDA nanoregulator to achieve distinctive targeting to the synovium region, and photocatalytic H_2 generation for selectively reducing cytotoxic ROS and the PTT for RA therapy.

damage [19]. Noticeably, the extremely low solubility of H_2 at physiological conditions limits its biological applications. How to achieve high photocatalytic H_2 production and targeted delivery is crucial for enhancing the efficacy of hydrogenothermal therapy, but it still remains challenging at present [20–25]. Nanomaterials are likely to provide a platform to overcome this challenge [26–30].

In recent years, the research of nanomaterials based on photocatalysis has developed rapidly, such as hollow semiconductor photocatalysts, tungsten-based photocatalysts, TiO_2, 1T-$MoSe_2$/g-C_3N_4 etc. As a fantastic semiconductor-like porousmaterials, metal-organic frameworks (MOFs), composed of a combination of organic linkers with metalions/clusters, have shown great potential in photocatalysis field [35–39]. Porous semiconductor materials facilitate the exposure of active centers. In addition to the above-mentioned advantages of MOFs, the crystalline nature of MOFs avoids the structural defects of the e-h recombination center. In order to further suppress e-h recombination, introducing metal nanoparticles (NPs) into n-type semiconductor MOFs is a proven method to promote charge separation. Because of the Schottky barrier, the migrated electrons are captured by the metal NPs, and the holes diffuse to the surface of MOFs. However, most MOFs have high conduction band (CB) and low valence band (VB) similar to semiconductors, which makes them have a wide band gap, which can only cause ultraviolet (UV) light absorption, limiting their biological applications. By introducing surface plasmon resonance (SPR), the light absorption of MOFs can be extended from UV to visible light (Vis) and even near infrared (NIR). The SPR of nanostructured metals such as Au and Ag can be excited by Vis to produce hot electrons and inject them into lowest unoccupied molecular orbital (LUMO) or CB of n-type semiconductor-like MOFs, which greatly improves e-h separation and photocatalytic efficiency [40–45]. Hai-Long Jiang et al. demonstrated that compared with other Pt-MOF and MOF@Au, under Vis irradiation, Pt-MOF@Au exhibits higher photocatalytic H_2 production rate [46,47]. We introduce Pt-MOF@Au as amultifunctional H_2 generators achieve the rheumatoid synovial cell-targeted delivery, exceptionally high photocatalytic H_2 production.

Herein, we designed the Pt-MOF@Au@QDs/PDA to realize the combination of photothermal therapy (PTT) and H_2 therapy of RA to passively target rheumatoid synovial sites by the "ELVIS" effect (extravasation through leaky vasculature and subsequent inflammatory cell-mediated sequestration) [48] (Scheme 1). Furthermore, the biodegradable polydopamine with remarkable photothermal conversion efficiencies and excellent biocompatibility has become a relatively non-invasive and gentle alternative for the treatment of diseased cells

or tissues. The Pt-MOF@Au results in the most effective strategies that extending their light absorption from UV to visible or even NIR region, which enables the visible light-guided production of H_2. In addition, due to the unique photophysical properties of perovskite quantum dots (QDs), they are used as fluorescent signals for positioning Pt-MOF@Au@QDs/PDA nanoparticles. Hence, the synergistic MOFs-guided production of H_2 and PTT based on the multifunctional Pt-MOF@Au@QDs/PDA may become an efficient treatment method to treat RA.

2. Materials and methods

2.1. Synthesis of Pt NPs

The Pt NPs were prepared by a hydrothermal synthesis [49,50]. Briefly, 20 mL of ethylene glycol was utilized to dissolve $H_2PtCl_6 \cdot 6H_2O$ (50.75 mg, 0.098 mmol) in a two-neck round bottom flask and 222 mg of poly(vinylpyrrolidone) (PVP, MW = 55,000) was added to the above solution and stir to completely dissolve. The mixture was put into a metal bath which was preheated to 180 °C and stir quickly for 10 min. PVP-protected Pt NPs were collected by centrifugation (8000 rpm, 5 min). In order to remove excrescent PVP, acetone and hexane were used to treat the above samples. Then the sample was re-dispersed in DMF.

2.2. Synthesis of Au

Au NPs were prepared according to the process similar to the above Au NRs [51], except with the following changes to the growth solution: 1) 9.0 g of CTAB was changed to be 3.5 g; 2) 5-bromosalicylic acid was replaced by 5-aminosalicylic acid; 3) 6 mL of 4 mM $AgNO_3$ was used instead that of 12 mL; 4) the added volume of 64 mM ascorbic acid solution was changed from 2 mL to 1 mL. Au NPs were collected by centrifugation (7000 rpm, 10 min), washed 2–3 times, and dried in a vacuum drying oven at 60 °C 20 mg of Au NPs were then weighed and redispersed in 10 mL of deionized water with concentration of 2 mg/mL for further use.

2.3. Synthesis of Pt-MOF

Pt-MOF was synthesized by adding Pt NPs into the reactants of MOF. Typically, $ZrCl_4$ (10.20 mg) was dissolved in 5 mL DMF, and terephthalic acid (14.50 mg) was dissolved in 5 mL DMF. Then the above two

solutions were added to a 20 mL flask, and then 1.2 mL of acetic acid and an appropriate amount of Pt NPs were added and sealed. The reaction was allowed to stand in an oven at 120 °C for 12 h, the product was collected by centrifugation, and the sample was washed 3 times with DMF. Then it was soaked in methanol solution for 24 h, and finally dried in an oven at 50 °C for 12 h.

2.4. Synthesis of Pt-MOF@Au@QDs

The Pt NPs, Pt-MOF and Au were prepared following the method described above. The as-synthesized Pt-MOF were immersed in a certain amount of stock solution of Au NRs and QDs. After being sonicated at room temperature for 2 h using a commercial ultrasonic cleaner, the precipitates were separated by centrifugation, washed with anhydrous methanol, and then dried at 50 °C under overnight.

2.5. Synthesis of Pt-MOF@Au@QDs/PDA

Prepare the 0.5–2 mg/mL dopamine aqueous solution, add Pt-MOF@Au@QDs (powdered), ultrasound (80–120 W, 30 min) at room temperature (20–30 °C), stir (10 min), centrifuge, and wash (deionized water, Wash with ethanol three times), and dry (80 °C, 12 h).

2.6. In vitro photothermal

We utilized thermal imaging camera to measure the in vitro temperature changes of saline and Pt-MOF@Au@QDs/PDA under different conditions. Briefly, put different materials into a test tube, irradiate them under 1.0 W cm^{-2} NIR light for 6 min, and use a thermal imaging camera to plot the temperature profile in vitro at different time points. In order to estimate the photothermal effect of different concentrations of Pt-MOF@Au@QDs/PDA, we introduced 1 mL of Pt-MOF@Au@QDs/PDA solution with different concentrations (2.5, 5, 7.5, 10, 12.5 μg/mL) into a quartz tube, and the 808 nm laser was used to irradiate nanoparticles for 6 min. In addition, by surveying changes in the temperature of the Pt-MOF@Au@QDs/PDA solution under the irradiation of 808 nm laser (0.5–1.5 W cm^{-2}), the photothermal heating curve of the sample solution was obtained. Besides, to evaluate the photothermal stability of Pt-MOF@Au@QDs/PDA, the Pt-MOF@Au@QDs/PDA was irradiated with 808 nm laser for 480 s, then the irradiation was stopped, and the irradiation was re-irradiated after an interval of 520 s, and the above operation was repeated 4 times.

2.7. Cytotoxicity assays

The perniciousnes of the Pt-MOF@Au@QDs/PDA toward RAW264.7 and HFLS-RA cell cloned strain was evaluated by standard (CCK-8) method in vitro. Typically, 100 μL of cell suspension containing approximately 5000 cells was seeded in each well of a 96-well plate and then incubated for 12 h. The initial medium was replaced with the medium comprising Pt-MOF, Pt-MOF@Au, Pt-MOF@Au/PDA and Pt-MOF@Au@QDs/PDA after the cells are attached. Then PBS was utilized to wash cells after further incubating for 24, 48 and 72 h. Subsequently, 100 μL of CCK-8 was added to each well, and then the cells were incubated for another 2 h. Finally, the microplate reader was utilized to detect the absorbance of each well at 450 nm. The following equation was utilized to calculate cell viability: cell viability = ([OD]test/[OD]control) × 100% [52].

2.8. Cellular experiments and intracellular endocytosis

HFLS-RA cells seeded in confocal dish were incubated in 2 mL of DMEM medium comprising 10 μg/mL Pt-MOF@Au@QDs/PDA for different time durations (1, 3, and 6 h). Then, PBS was utilized to wash HFLS-RA cells twice and the lysosome was stained with Lysotracker RED DND-99 for 30 min. Subsequently, HFLS-RA cells were washed twice

again and fixed with 4% paraformaldehyde reagent, and the DAPI was utilized to stained nucleus for 8 min After these operations, in order to remove the dye, cells were rinsed with PBS. Finally inspected under the confocal laser scanning microscope.

2.9. Live/dead cells staining

The HFLS-RA cells or RAW264.7 cells were cultivated in 96-well plates for 24 h. Then the cells were incubated in complete medium containing Pt-MOF@Au@QDs/PDA at concentration of 10 μg/mL. Subsequently, HFLS-RA cells which were divided into five groups were received the exposure of 808 nm laser, or 808 nm laser combined with visable light for 6 min. The control group was cells treated with saline. Ultimately, the CCK-8 assay was utilized to detect cell viability and calculated cell viability by equation mentioned above: cell viability = ([OD]test/[OD]control) × 100%.

2.10. Photothermal imaging

The infrared thermal camera was utilized to perform infrared thermal imaging in vivo with the 808 nm excitation laser. We induced arthritis in DBA1/J mice utilizing the method given in the Kyung-Hwa Yoo literature [53]. *In vivo* photothermal imaging was performed for RA after random grouping: (i) RA mice treated with PBS; (ii) RA mice injected (i.v.) with Pt-MOF@Au@QDs/PDA (10 μg/mL) + NIR irradiation; (iii) RA mice injected (i.v.) with Pt-MOF@Au@QDs/PDA (10 μg/mL) + NIR-visible light irradiation. After the above treatment, the laser(1.0 W/cm^2) was taken advantage of irradiating the arthritis area for a period of time, and then real-time photothermal imaging was performed to record the photothermal imaging at different time points (0, 2, 4, 6 min).

In addition, we investigated the photothermal effect of Pt-MOF@Au@QDs/PDA in vitro. We distinguished live/dead cells by the fluorescent color which was produced by the photoablation inducing live/dead experiment. Particularly, HFLS-RA cells were planted in a 12-well plate and incubated overnight. Subsequently, aspirate the original medium and incubate the cells with fresh medium containing Pt-MOF@Au@QDs/PDA. Subsequently, the cell were exposed to NIR or NIR-Vis for 6 min. After incubating for 12 h, PBS was utilized to wash the cells gently three times and added the calcein AM/PI solution, and incubated at 25 °C for 40 min in the dark, after which replaced the calcein AM/PI solution with 100 μL of PBS. Finally, the fluorescent assay was utilized to observe the mouse arthritis synovial cells by the inverted fluorescence microscope.

2.11. Fluorescence imaging

After CIA mice received a tail vein injection of Pt-MOF@Au@QDs/PDA (10 μL, 5 mg/kg), 4% chloral hydrate was utilized to anesthetize the mice and remained anesthetized until the end of the experiment. Finally, the imaging system is utilized to detect the fluorescent imaging in vivo at the 640 nm excitation wavelength after 1, 6, 12 and 24 h post-injection.

2.12. Induction and treatment of rheumatoid arthritis

The rheumatoid arthritis was induced according to the method reported by Kyung-Hwa Yoo. Briefly, absolutely mixed the bovine type II collagen emulsion and complete Freund's adjuvant in equal volumes, and the collagen-induced rheumatoid arthritis (CIA) mouse model was induced by subcutaneous injection of 400 μL mixed emulsion into the base of the tail of male DBA1/J mice. Next, at 21 days after the initial immunization, 200 μL of the mixed emulsion was injected in the same way. After successful induction of the CIA mouse model, saline (group 1), Pt-MOF@Au@QDs/PDA (group 2, 3 and 4) was injected into the mice through the tail vein. After the tail vein injection of composite nanoparticles, mice in group 3 were irradiated with NIR for 6 min, and mice in
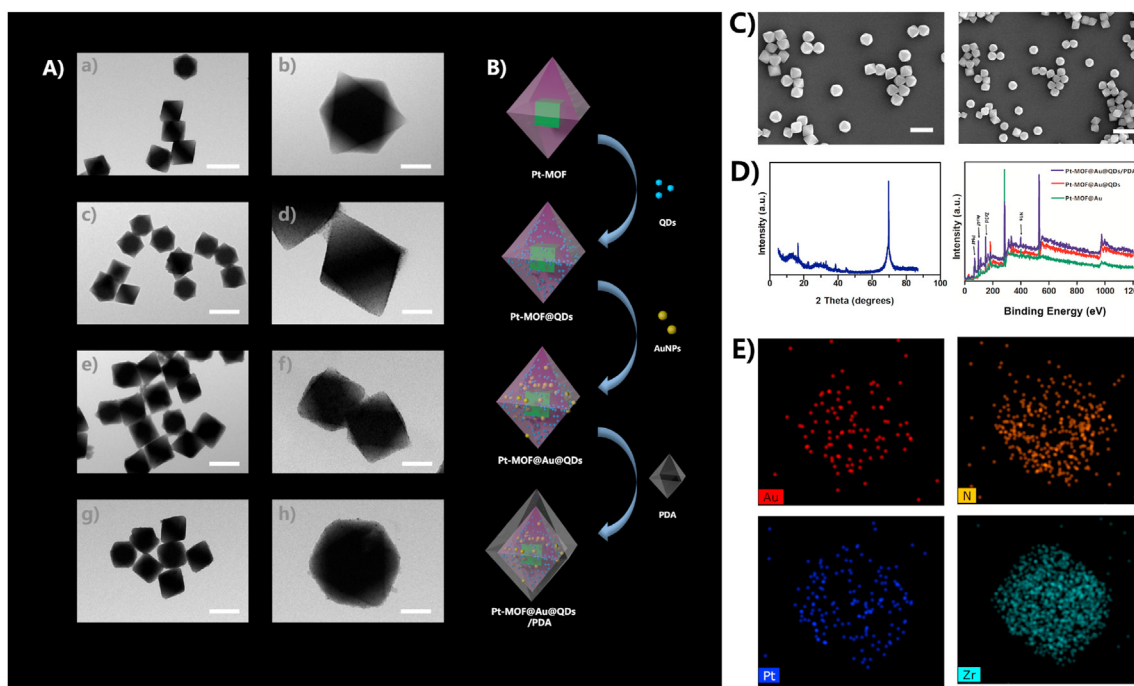
Fig. 1. (A) Representative TEM images of (A-a, A-b) Pt-MOF, (A-c, A-d) Pt-MOF@ QDs (A-e, A-f), Pt-MOF@Au@QDs (A-g, A-h), Pt-MOF@Au@QDs/PDA; (B) Schematic illustration of major synthetic procedures in Pt-MOF@Au@QDs/PDA fabrication; (C) SEM of Pt-MOF@Au@QDs/PDA; (D) XPS spectra of Pt-MOF@Au@QDs/PDA, powder XRD patterns of Pt-MOF@Au, Pt-MOF@Au@QD and Pt-MOF@Au@QDs/PDA; (E) The corresponding EDX elemental mapping of Pt-MOF@Au@QDs/PDA.

group 4 were irradiated with NIR and Vis light at the same time. After the tail vein injection, the mice were observed every 5 days until 25 days, while carefully recording the clinical index of paws during the treatment period [54].

2.13. Histopathological

The mice were euthanized 56 days after the initial immunization, the swollen ankle and knee joints were collected, and the soft tissues and muscles around the joints were removed, fixed with 4% para-formaldehyde solution for 7 days. Subsequently, 5% formic acid was utilized to decalcify for 3 days. Then, PBS was utilized to wash samples thoroughly and paraffin was utilized to embed samples, and 4 μm thick paraffin sections were cut. Ultimately, joint sections were stained with H&E, and synovial hyperplasia and osteoclasia changes were observed by microscope.

2.14. Statistical analysis

The statistical analyses were mainly conducted by Student's t-test. Differences were considered statistically significant at *$p < 0.05$ (**$p < 0.01$).

3. Results and discussion

3.1. Characterization of Pt-MOF@Au@QDs/PDA

As we saw in the schematic illustration for the synthesis of Pt-MOF@Au@QDs/PDA (Fig. 1B), Pt-MOF and QDs were presynthesized based on the documented methods [55]. The details of QDs producing course process were diaplayed in Fig. S2. The Pt NPs were evenly dispersed on the outer surface of the entire MOF (Fig. 1Aa-1Ab). However, when the MOF structure was holonomic, most of the Pt NPs remained in the reaction solution without being reduced. That was because the reducibility of DMF was weak in the absence of H_2 (Fig. 1A).

Therefore, these Pt NPs which were dispersed on the external surface of the MOF, but were not encapsulated can be removed by washing and centrifugation, which often led to uneven distribution of Pt NPs and low loading rate. The TEM images showed the successful synthesis of highly monodispersed octahedral crystals containing Pt-MOF@QDs, Pt-MOF@Au@QDs and Pt-MOF@Au@QDs/PDA (Fig. 1Ac-1Ad). The results were consistent with the morphology of the octahedral Pt-MOF crystal, which indicated that the incorporation of QDs, Au and PDA had almost no effect on the Pt-MOF formation. SEM images showed a highly dispersed octahedral Pt-MOF@Au@QDs/PDA crystal, which further illustrates that the incorporation of QDs, Au and PDA did not affect Pt-MOF formation (Fig. 1C). HAADF-STEM imaging and corresponding EDX elemental mapping (Fig. 1E) further demonstrated that Au NPs were also evenly distributed on the entire surface of the Pt-MOF. Typical Au NPs dispersion in the materials was in the range of 53–71%. Most of Pt NPs were dispersed on the outer surface of the MOF, which may be due to the diffusion resistance of the inner and outer surfaces of the MOF, which further proved the importance of confinement effect provided by surrounding MOF shell. Furthermore, in our TEM observations, no significant changes were observed in the measurement and distribution of metal nanoparticles and the configuration of the Pt-MOF. The characteristic XRD peaks of Pt-MOF@Au@QDs/PDA composites matched well with those of the parent Pt-MOF (Fig. 1D), indicating that the incorporation of QDs, Au and PDA did not affect configuration of MOF. In addition, the characteristic peaks of Pt NPs were relatively low, which may be caused by the small particle size or the low content of Pt.

3.2. In vitro photothermal effect

The photothermal property of Pt-MOF@Au@QDs/PDA was systematically researched. As shown in Fig. 2A and Fig. 2B, when irradiated with an 808 nm laser, the temperature of the Pt-MOF@Au@QDs/PDA suspension increased significantly, which highly depends on the irradiation duration. When the Pt-MOF@Au@QDs/PDA suspension was irradiated with or without Vis for 6 min, the temperature of the suspension
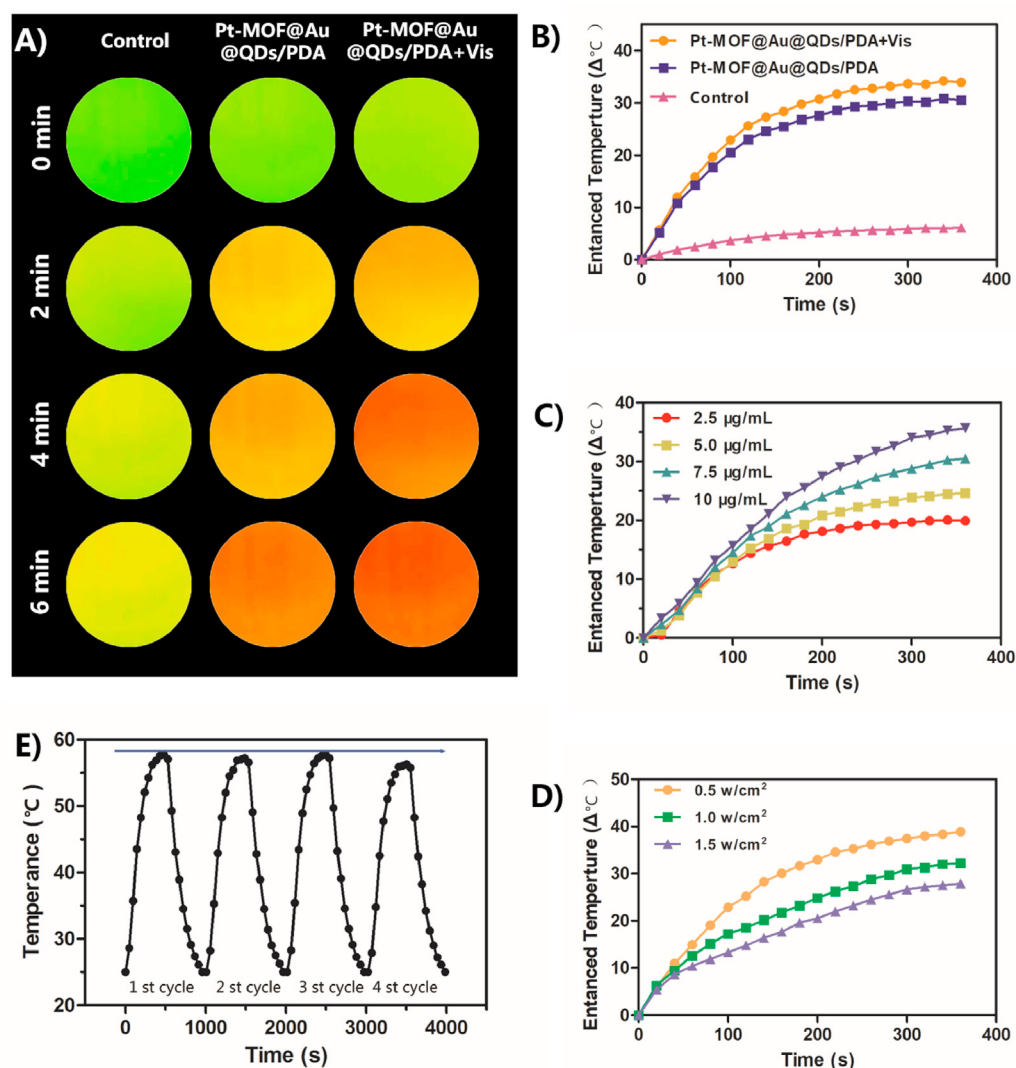
Fig. 2. Thermal images of the PBS, Pt-MOF@Au@QDs/PDA with or without Vis, aqueous suspension under 1 W/cm^2 808 nm laser from 0 to 6 min; (B) Photothermal heating curve of water dispersion under different conditions (NIR or NIR-Vis); Control was water (C) Photothermal heating curves of the Pt-MOF@Au@QDs/PDA aqueous dispersions with increasing concentrations (2.5, 5, 7.5 and 10 μg/mL) upon 808 nm laser irradiation; (D) Temperature profiles of Pt-MOF@Au@QDs/PDA aqueous dispersions (10 μg/mL) under different power intensities (0.5, 1.0 and 1.5 W/cm^2); (E) The temperature curve of 10 μg/mL Pt-MOF@Au@QDs/PDA water dispersions over 4 cycles with 808 nm laser(1 W/cm^2).

respectively increased by 32.3 °C and 29.3 °C. In contrary, pure deionized (DI) water as a control group was only observed the 5 °C temperature elevation. By comparison with Pt-MOF@Au@QDs/PDA without Vis, Pt-MOF@Au@QDs/PDA with Vis exhibited relatively stronger NIR-photothermal effects (Fig. 2B), which indicated that the photothermal effect was enhanced by the local H$_2$ generation. Furthermore, the photothermal conversion efficiencies (η) of Pt-MOF@Au@QDs/PDA with or without Vis were measured to be as high as 64.8% and 62.9% by taking advantage of the calculation formula previously reported by Zink [56]. The specifics of calculation procedure were exhibited in Fig. S1. As indicated in Fig. 2C, Pt-MOF@Au@QDs/PDA solution exhibited a concentration-dependent photothermal performance. It is noteworthy that the temperature of Pt-MOF@Au@QDs/PDA suspension with a concentration of 10 μg/mL rapidly increased by 36.7 °C within 6 min under laser irradiation. As given in Fig. 2D, as the laser power increases from 0.5 to 1.5 W/cm^2, temperature elevation (ΔT) of ~27.5, 32.9, and 39.8 °C were observed, suggesting that the temperature elevation was positively correlated with the laser power density. These results indicated that the Pt-MOF@Au@QDs/PDA exhibited excellent photothermal conversion efficiency under NIR laser irradiation. In order to further illustrate photothermal stabilization and transduction efficiency of Pt-MOF@Au@QDs/PDA, as shown in Fig. 2E, the 808 nm laser (1 W/cm^2) was used to continuously irradiate the Pt-MOF@Au@QDs/PDA

dispersion (10 μg/mL) for 6 min (laser ON), and then turned off the laser to make the Pt-MOF@Au@QDs/PDA dispersion is naturally cooled to surrounding temperature (laser OFF). The heating-cooling curve illustrated that the Pt-MOF@Au@QDs/PDA had excellent stabilization and reproducibility even after they were irradiated for several cycles. Collectively, these results illustrated that Pt-MOF@Au@QDs/PDA was potentially suitable PTT nanoagents.

3.3. Cellular internalization and in vitro cytotoxicity assay

As a prerequisite, the efficient cellular internalization is vital for guaranteeing sufficient therapeutic effect on HFLS-RA cells. The internalization of Pt-MOF@Au@QDs/PDA was evaluated in HFLS-RA cells at various time intervals utilizing confocal laser scanning microscopy (CLSM). Schematic illustration of internalization mechanism of Pt-MOF@Au@QDs/PDA into HFLS-RA cells through "ELVIS" effect was exhibited in Fig. 3A. The CCK-8 assay was utilized to assess potential cytotoxicity of the Pt-MOF@Au@QDs/PDA and synthetic intermediate product for further examining the biological applicability of the fabricated nanoparticle. The cell viability data exhibited in Fig. 3B and C illustrated that the newly constructed Pt-MOF@Au@QDs/PDA nanoparticles did not significantly cause cellular deaths of HFLS-RA cells. Observably, cell viability was about 91% at 72 h incubation with Pt-
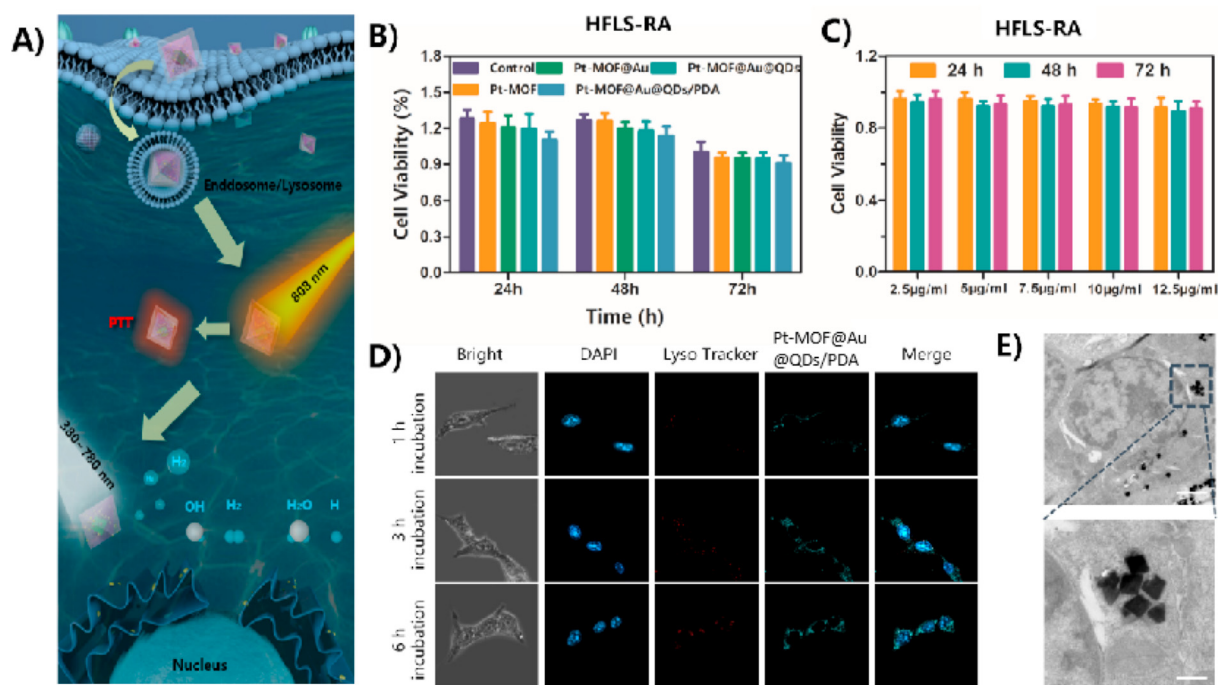
Fig. 3. (A) Schematic illustration of cell internalization pathway, H_2 production in situ and the PTT of Pt-MOF@Au@QDs/PDA nanoplatform for RA treatment; (B) Cell viability of HFLS-RA cells incubated with various materials measured by the CCK-8 assay; (C) Cell viability of HFLS-RA cells incubated with different concentrations of Pt-MOF@Au@QDs/PDA measured by the CCK-8 assay; (D) Intracellular fluorescence of Pt-MOF@Au@QDs/PDA in HFLS-RA cells was observed utilizing CLSM at the different time points after incubation with Pt-MOF@Au@QDs/PDA(10 μg/mL); (E) TEM photographs of the Pt-MOF@Au@QDs/PDA engulfed by HFLS-RA cells and subcellular distribution of the Pt-MOF@Au@QDs/PDA, Scale bar: 500 nm and 200 nm.
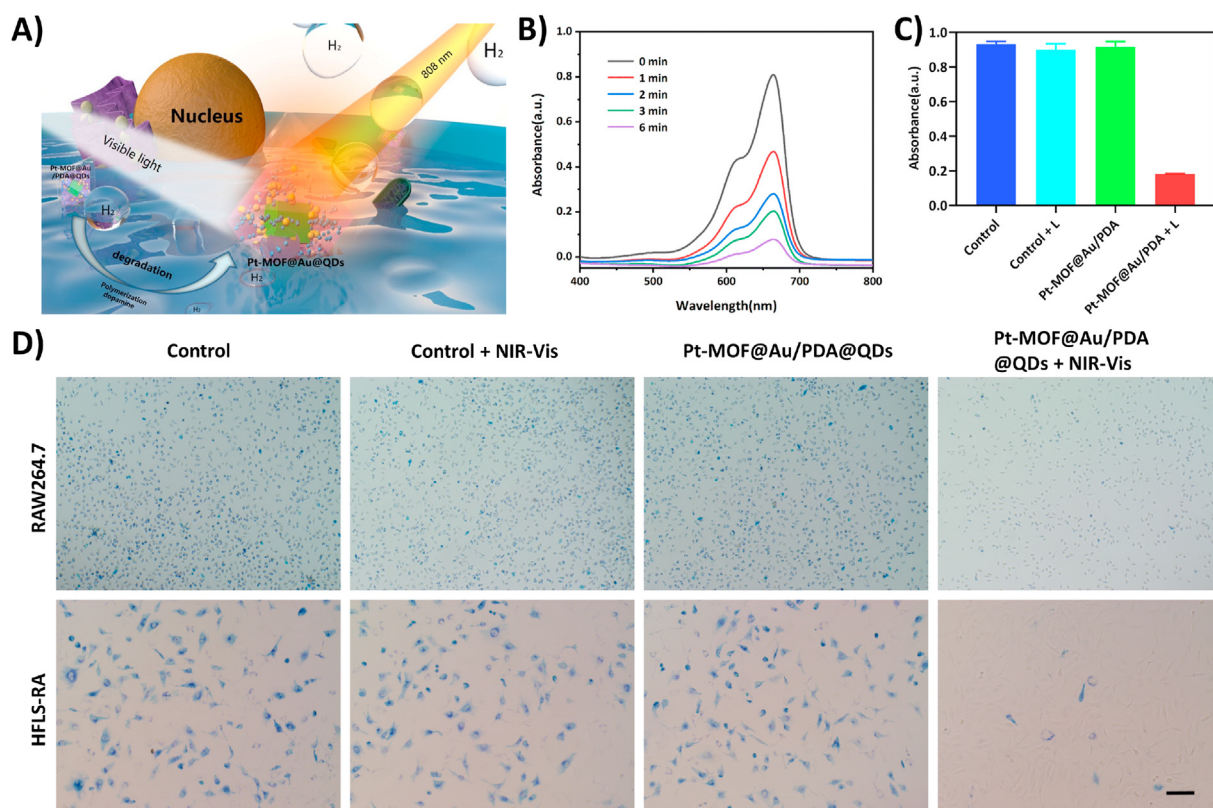

Fig. 4. (A) Schematic illustration of photocatalytic H_2 production of Pt-MOF@Au@QDs/PDA in cells; (B) Absorbance of MB solution containing Pt-MOF@Au@QDs/PDA nanoparticles at 664 nm under different NIR-Vis laser radiation times(0, 1, 2, 3, 6 min); (C) Absorbance at 664 nm of HFLS-RA cells stained with MB in different treatments; (D) Qualitative survey of reductive H_2 production in MB-stained HFLS-RA cells and RAW264.7 cells in different treatments(Scale bar: 100 μm).
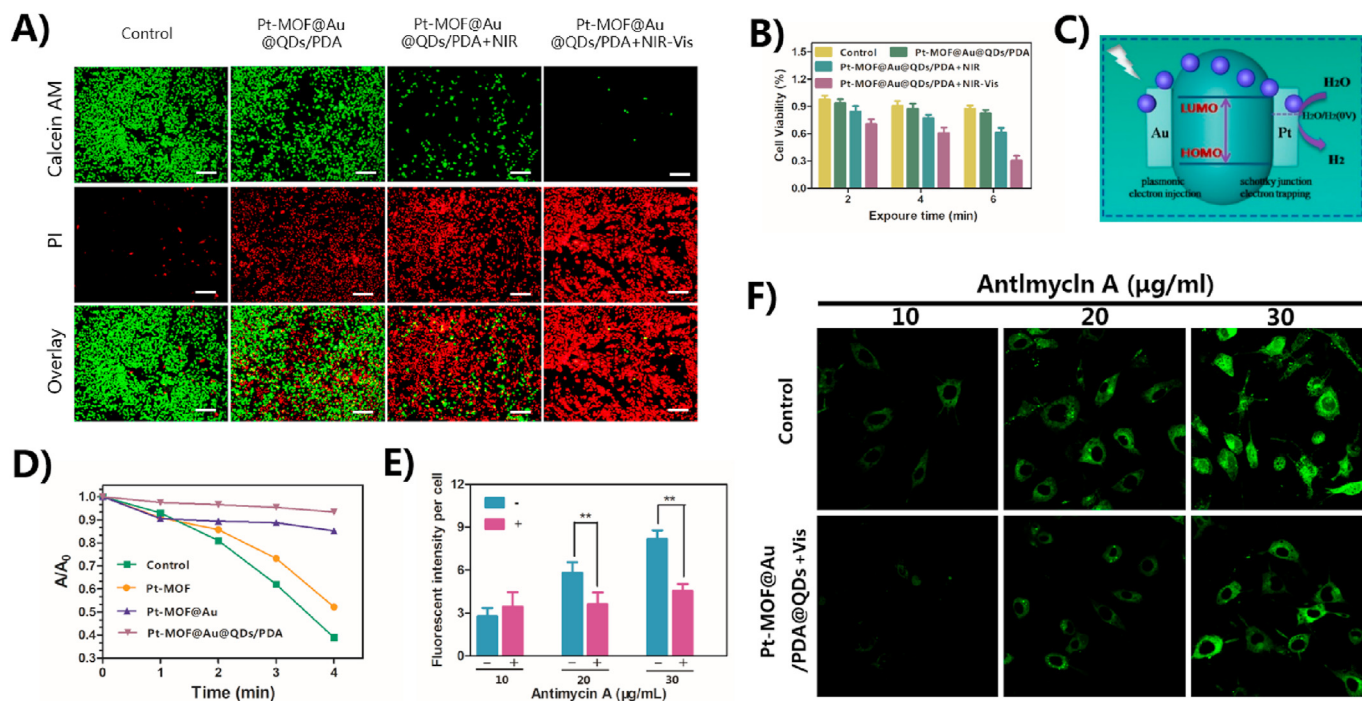
Fig. 5. (A) Results of Calcein AM/PI costained HFLS-RA cells after different managements by fluorescence microscopy. Green and red represent live and dead cells, respectively (Scale bar: 100 μm); (B) Cell viability of HFLS-RA cells treated with Control, Pt-MOF, Pt-MOF@Au, Pt-MOF@Au@QDs and Pt-MOF@Au@QDs/PDA; (C) Schematic illustration showing the electron migration at the two metal-MOF interfaces based on the energy levels; (D) Decomposition rates of ABDA in the presence of Pt-MOF@Au and Pt-MOF@Au@QDs/PDA under light irradiation, where A_0 and A are the absorbances of ABDA at 378 nm; (E) HPF fluorescence in cells treated with antimycin A with or without 0.6 mM H_2. *P < 0.05, **P < 0.01. (F) Representative laser-scanning confocal images of the fluorescence of the OH marker HPF were taken 30 min after the addition of antimycin A. (For interpretation of the references to color in this figure legend, the reader is referred to the Web version of this article.)

MOF@Au@QDs/PDA NPs, which showed the good biocompatibility of these NPs (Pt-MOF, Pt-MOF@Au@QDs, or Pt-MOF@Au@QDs/PDA). In addition, the concentration-dependent cytotoxicity of Pt-MOF@Au@QDs/PDA in HFLS-RA cells over 24 h, 48 h and 72 h were tested utilizing CCK-8 assay. As illustrated in Fig. 3C, the cell viability against HFLS-RA cell lines was still maintained above 90% even at a Pt-MOF@Au@QDs/PDA concentration of 12.5 μg/mL. These results illustrated that Pt-MOF@Au@QDs/PDA had perfect biocompatibility and can serve as potential photothermal agents for biological applications. Fig. 3D shown the cyanic fluorescent signal originated from QDs continuously increased with the extension of incubation time. This confirmed more Pt-MOF@Au@QDs/PDA were engulfed into HFLS-RA cells through endocytosis pathway. In addition, it was worth noting that after 1 h and 3 h of incubation, the green fluorescence was mainly distributed in the lysosomes marked by LysoTracker Red, and after 6 h, the green fluorescence was gradually transferred to the entire cytoplasm of HFLS-RA cells. Meanwhile, the colocalization of Pt-MOF@Au@QDs/PDA with lysosomes noticeably diminished at 6 h, evidenced by the phenomenon that most red fluorescence of lysosomes separated with the green fluorescence from Pt-MOF@Au@QDs/PDA. This observed translocation revealed that the lysosomal escape of Pt-MOF@Au@QDs/PDA was extremely significant to occur in HFLS-RA cells during the treatment time. Meanwhile, the biological transmission electron microscope was utilized to observe subcellular location and distribution of Pt-MOF@Au@QDs/PDA. As shown in Fig. 3E, consistent with the CLSM inspection, the Pt-MOF@Au@QDs/PDA was distributed in the cytoplasm and trapped in the cytoplasmic vesicles of HFLS-RA cells after 6 h incubation. These indicated high internalization of Pt-MOF@Au@QDs/PDA by HFLS-RA cells, which is necessary for effective treatment and alleviation of RA. In addition, the internalization and in vitro cytotoxicity of Pt-MOF@Au@QDs/PDA were further evaluated. The results were diaplayed in Fig. S3.

3.4. Photocatalytic hydrogen production

Methylene blue (MB) has been universally utilized to catalyze quickly detect H_2. Blue MB could be attenuated to colorless leucomethylene blue through the photocatalytic H_2 production of Pt-MOF@Au@QDs/PDA nanoparticles. After confirming the successful synthesis of Pt-MOF@Au@QDs/PDA nanoparticles, we used MB to detect photocatalytic H_2 production of Pt-MOF@Au@QDs/PDA nanoparticles in vitro and in cells. Thereinto, the intensity change of the MB characteristic absorption at 664 nm noted by an ultraviolet spectrophotometer can be adopted to evaluate the amount of photocatalytic H_2 production. As shown in Fig. 4A, the schematic illustration of photocatalytic H_2 production of Pt-MOF@Au@QDs/PDA nanoparticles in cells. From Fig. 4B, the absorbance of MB at 664 nm decreased with the increase of NIR-Vis laser irradiation time, which indicated that with the increase of NIR-Vis laser irradiation time, the photocatalytic hydrogenation content of in vitro increases. As shown in Fig. 4C, after treatment with Pt-MOF@Au@QDs/PDA nanoparticles, the absorbance at 664 nm of the HFLS-RA cells stained with MB was significantly reduced, indicating that photocatalytic hydrogen production also exists in the cells. Visually, after treatment with the Pt-MOF@Au@QDs/PDA + NIR-Vis, the MB-stained HFLS-RA cells and RAW264.7 cells observably faded out, meaning the evidently reduction of MB (Fig. 4D). Both results in solution and cells affirmed that Pt-MOF@Au@QDs/PDA nanoparticles possessed remarkable bio-reductivity, which could enable the effective reducing of RA microenvironment overexpressed •OH.

3.5. Combined phototherapeutic efficiency and H₂ selectively reduces OH in cultured cells

Given the intriguing photothermal efficiency, the CCK-8 assay was also taken advantage of estimating the effect of in vitro PTT of the Pt-

MOF@Au@QDs/PDA under different conditions (Fig. 5B). The HFLS-RA cells were treated with saline or Pt-MOF@Au@QDs/PDA, with 808 nm laser treatment or not. The viability of cells radiated by visible light and 808 nm laser was evidently lower than those treated with 808 nm laser only at the equivalent concentration, which proved that the synergistic PTT effect of H_2 was more effective than PTT alone. Furthermore, in order to further verify the efficacy, after receiving different treatments, fluorescence staining of both living and dead cells was performed with Calcein-AM and PI, showing dead cells (red) and live cells (green). As shown in Fig. 5A, Compared to the control or Pt-MOF@Au@QDs/PDA and Pt-MOF@Au@QDs/PDA + NIR group, the HFLS-RA cells exhibited the strongest red fluorescence and the weakest green fluorescence after being incubated with the Pt-MOF@Au@QDs/PDA and then irradiated by NIR and visible light at the same time, which confirmed that combination of H_2 therapy and traditional PTT therapy have synergetic therapy effects, which was consistent with the above cell viability results. As exhibited in Fig. 5C, the schematic illustration of band alignments and charge flow at the two metal-MOF interfaces.

To affirm that H_2 protects against $-O_2$, the menadione, a mitochondrial complex I inhibitor, was added to cells to induce $-O_2$ production. As exhibited in Fig. 5D, the absorbance at 378 nm of ABDA treated with Pt-MOF@Au and Pt-MOF@Au@QDs/PDA under light irradiation exhibited a significant attenuation. It is worth noting that after 4 min of visible light irradiation, the absorbance of ABDA treated with Pt-MOF@Au@QDs/PDA solution dropped by 61%, suggesting that 6.1 μmol of ABDA was depleted every min when Pt-MOF@Au@QDs/PDA(10 μM) was exposed to the light. These results indicated that Pt-MOF@Au@QDs/PDA can protected cells from peroxidation.

H_2 reduces the ·OH produced by radiolysis or photolysis of water; however, whether H_2 can effectively neutralize ·OH in living cells has not been directly investigated. The ·OH produced spontaneously by the cell which causes cellular damage is not sufficient to be detectable, therefore, we used antimycin A, an inhibitor acting on mitochondrial respiratory complex III, to treat the cell, which can rapidly convert the $-O_2$ in the cell into H_2O_2. According to Ref. [57], the addition of antimycin A increased levels of $-O_2$ and H_2O_2, as judged by the fluorescence signals emitted by the oxidized forms of MitoSOX and 2′,7′-dichloro dihydro fluorescein (H_2DCF), respectively. As show in Fig. 5E and F, H_2 treatment significantly decreased levels of ·OH, which was assessed by the fluorescence signal emitted by the oxidized form of 2-[6-(4′-hydroxy) phenoxy-3H-xanthen-3-on-9-yl] benzoate (HPF). In the absence of H_2, when we utilized antimycin A to treat cells, the HPF signals increased both in the nuclear and cytoplasm. This may be due to the diffusion of H_2O_2 from the mitochondria to produce ·OH. Notably, H_2 decreased ·OH levels even in the nuclear region (Fig. 5E and F).

3.6. In vivo NIR-Photothermal effect and fluorescence imaging

Moreover, the NIR photothermal effect of Pt-MOF@Au@QDs/PDA in the CIA model was checked, founding of CIA mice model and treatment process is shown schematically in Fig. 6A. At 1 h after the injection of Pt-MOF@Au@QDs/PDA (10 μg mL^{-1}, 100 μL) in the tail vein, the mice were anesthetized, and then the paws were illuminated with laser (1.0 W cm^{-2}) for 6 min. As exhibited in Fig. 6C, the thermal imaging camera was utilized to monitor the changes in the claw temperature. As shown in Fig. 6B and D, after 6 min of laser irradiation, the PBS control group only had a temperature increase of about 4.5 °C, while Pt-MOF@Au@QDs/PDA + NIR-Vis and Pt-MOF@Au@QDs/PDA + NIR groups exhibited a temperature increase of about 29 °C and 23.5 °C, respectively. This illustrated that Pt-MOF@Au@QDs/PDA + NIR-Vis and Pt-MOF@Au@QDs/PDA + NIR had excellent photothermal effects in vivo for thermal therapy of RA.
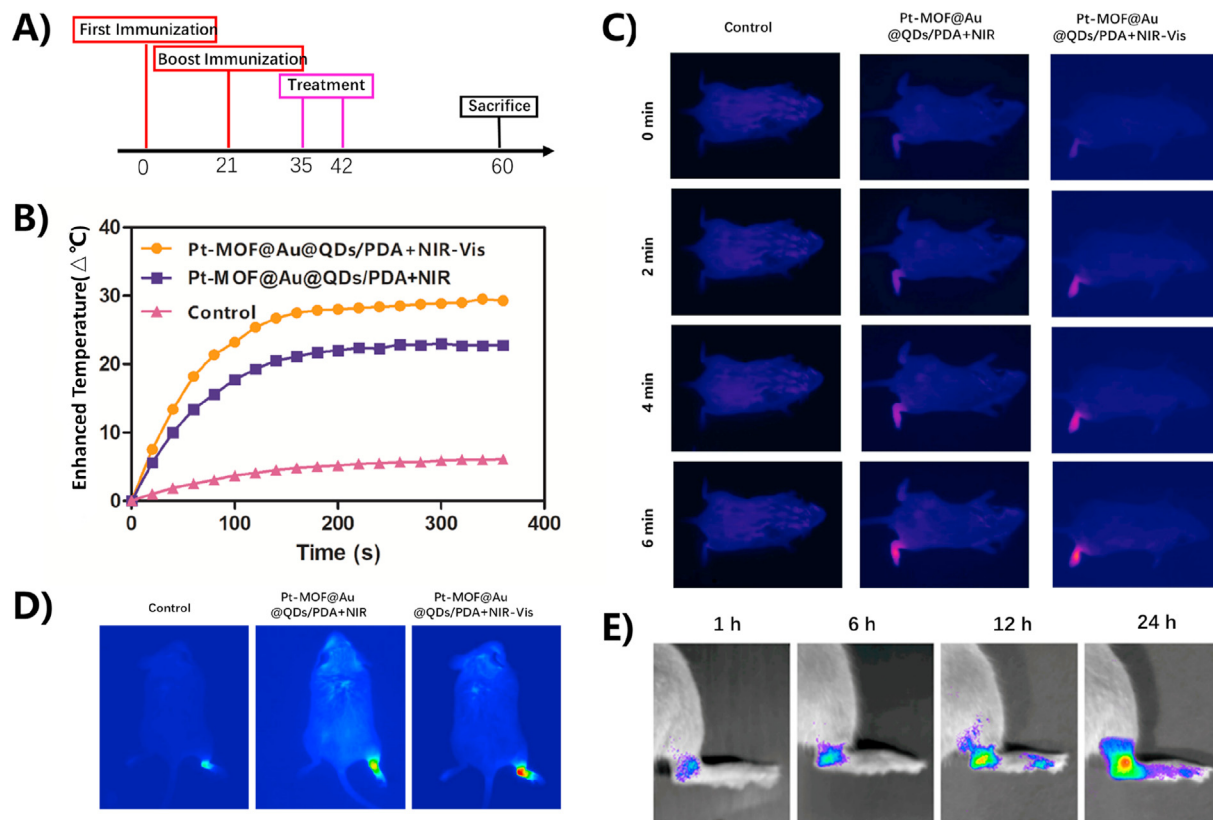

Fig. 6. (A) Founding of CIA mice model and treatment process; (B, D) The various parameters photothermal imaging of ankle joint on CIA mice (n = 3); (C) The various exposure time photothermal imaging of ankle joint on CIA mice (n = 3); (E) In vivo fluorescence imaging of Pt-MOF@Au@QDs/PDA in mice after intravenous injection at various time intervals.
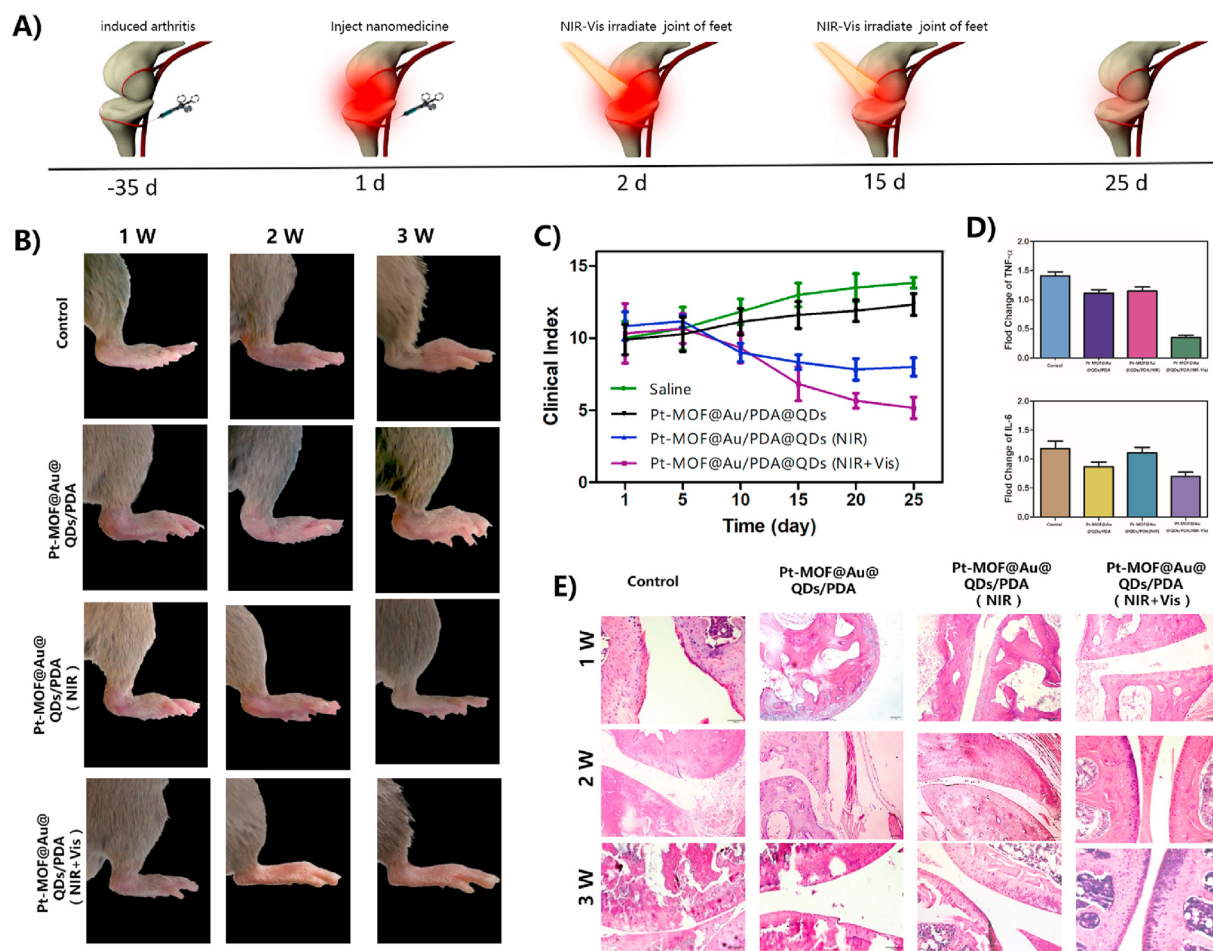
Fig. 7. (A) CIA mice therapy approach; (B) The lateral and anterior images of affected joints of CIA models after the treatment Pt-MOF@Au@QDs/PDA treatments with or without NIR + Vis irradiation at 1and 3 weeks; (C) The arthritic index of Pt-MOF@Au@QDs/PDAl with or without NIR + Vis irradiation; (D) Semiquantitative analysis of immunohistochemical staining for IL-6 and TNF-α in CIA mice. The bars represent the standard deviation. Asterisks (*) represent significance compared to untreated mice with *p < 0.05 (n = 5); (E) Effects of Pt-MOF@Au@QDs/PDA treatments with or without NIR + Vis irradiation at 1and 3 weeks on histopathological changes of inflamed joints. Scale bar: 200 μm.

In order to confirm the biodistribution and "ELVIS" effect of the Pt-MOF@Au@QDs/PDA in vivo, we injected the Pt-MOF@Au@QDs/PDA through the tail vein of mice, and then analyzed the in vivo biodistribution of the Pt-MOF@Au@QDs/PDA through the images. As shown in Fig. 6E, fluorescence of the Pt-MOF@Au@QDs/PDA was detected in the joint synovium about 1 h after the injection, and the fluorescence signal increased over time, which suggested that Pt-MOF@Au@QDs/PDA was effectively accumulated and retained in the joint synovium site. The fluorescent signal reached strongest about 24 h after injection, which may be due to the "ELVIS" effect. The fluorescence signal at this time was very beneficial for in vivo hydrogenothermal therapy.

3.7. Induction and treatment of rheumatoid arthritis

To evaluate therapeutic effect of the Pt-MOF@Au@QDs/PDA, we conducted an efficacy effect study and histopathological analyses. As to NIR-Vis irradiation groups, after the Pt-MOF@Au@QDs/PDA were injected, NIR-Vis was utilized to irradiate the mouse paws site at fixed time points, as shown in Fig. 7A. From Fig. 7B, severe deformities and swelling were observed throughout the multiple joints including paws in the saline + NIR and Pt-MOF@Au@QDs/PDA group. However, the paws in the Pt-MOF@Au@QDs/PDA + NIR group and Pt-MOF@Au@QDs/PDA + NIR-Vis group were reduced significantly swelling and flare. Especially Pt-MOF@Au@QDs/PDA + NIR-Vis group, it was almost the

same as normal joints without deformity and swelling. During the observation period, we carefully recorded CIA mice clinical index every 5 days (Fig. 7C). We found that in the first 5 d after treatment, there was no significant difference in the clinical indicators of the four groups. Then, compared with the saline and Pt-MOF@Au@QDs/PDA group, the clinical index began to decline in Pt-MOF@Au@QDs/PDA + NIR group and Pt-MOF@Au@QDs/PDA + NIR-Vis group, especially the clinical index in Pt-MOF@Au@QDs/PDA + NIR-Vis group decreased significantly after 15 days of injection, which may be related to PDA degradation and H_2 production.

In order to verify the efficacy of the targeted hydrogenothermal therapy, histological examinations of joints were performed. Pro-inflammatory cytokines including IL-6 and TNF-α play an important role in the pathological process of RA, and their high expressions are closely associated with the activity of RA. Immunohistochemical staining illustrated that IL-6 and TNF-α were highly expressed around the joints in group 1, while they were significantly reduced in group 4 (Fig. 7D).

These experiments were supporting our results suggesting that Pt-MOF@Au@QDs/PDA can effective treatment of RA. We utilized the histological of hematoxylin and eosin (H&E) staining to assess the efficacy of Pt-MOF@Au@QDs/PDA and the inflammation and erosion degree of bone and cartilage. RA model mice managed with PBS revealed critical synovial tissue hyperplasia and erosion of bone and cartilage, which demonstrated no significant therapeutic effect (Fig. 7E). The mice treated with Pt-MOF@Au@QDs/PDA with NIR irradiation not only

remarkably reduced the degree of synovial tissue proliferation, but also showed a significant improvement in the erosion of bone and cartilage. Expressly, CIA mice managed with Pt-MOF@Au@QDs/PDA with NIR + Vis illumination resulted in the smooth articular facet between cartilage and bone. There is, in addition, one further point to make. The potential toxicity of the Pt-MOF@Au@QDs/PDA has also been systematically estimated in vivo. The 15 male DBA1/J mice (6 weeks old) were randomly divided into 3 groups: (1) control group without management, (2) Pt-MOF@Au@QDs group, and (3) Pt-MOF@Au@QDs/PDA group. At 8 days after injection of different materials in the tail vein, the internal organs of the different groups of mice, including liver, spleen, kidney, heart and lung, were stained with H&E. Fig. S4 demonstrates that there are no obvious pathological changes in various organs between different groups, indicating that Pt-MOF@Au@QDs/PDA have insignificant toxicity in vivo.

4. Conclusions

We designed the Pt-MOF@Au@QDs/PDA to realize the combination of hydrogenthermal therapy of RA to passively target rheumatoid synovial sites by the "ELVIS" effect. The Pt-MOF@Au catalyzer combines Au's surface plasmon resonance excitation with Pt-MOF Schottky junction, and exhibits extremely efficient photocatalytic H_2 production under visible light irradiation. The PDA-mediated PTT which can buffering oxidative stress while removing proliferating synovial cells. Of note, by combined hydrogenothermal therapy, the side effect of pure thermal therapy to normal cells/tissues could be reduced while its buffering oxidative stress to synovial cells could be enhanced by the controlled administration of bio-reductive hydrogen. Such homoeostatic regulation function of bio-reductive hydrogen is similar to several typical therapeutic gases such as NO and CO, while H_2 is highly bio-safe without obvious poisoning effect. These results demonstrate that the multifunctional Pt-MOF@Au@QDs/PDA is an excellent and effective strategy for maximizing the therapeutic efficacy in the RA.

Author contributions

Wenzhen Pan: Methodology, Investigation, Formal analysis, Writing – original draft. Zheng Li: Methodology, Investigation, Formal analysis, Writing – original draft. Shang Qiu: Methodology, Investigation. Chengbai Dai: Software. Shengyue Wu: Software. Xin Zheng: Software. Fenglei Gao: Conceptualization, Funding acquisition, Methodology, Supervision, Writing-review. Ming Guan: Conceptualization, Funding acquisition, Methodology, Supervision, Writing-review.

Declaration of competing interest

The authors declare that they have no known competing financial interests or personal relationships that could have appeared to influence the work reported in this paper.

Acknowledgements

Appendix A. Supplementary data

Supplementary data to this article can be found online at https://doi.org/10.1016/j.mtbio.2022.100214.

References

[1] J.S. Smolen, D. Aletaha, I.B. McInnes, Rheumatoid arthritis, Lancet 388 (2016) 2023–2038, https://doi.org/10.1016/S0140-6736(16)30173-8.

[2] X. Bosch, Dendrimers to treat rheumatoid arthritis, ACS Nano 5 (2011) 6779–6785, https://doi.org/10.1021/nn203190x.

[3] J. Peiró Cadahía, J. Bondebjerg, C.A. Hansen, V. Previtali, A.E. Hansen, T.L. Andresen, M.H. Clausen, Synthesis and evaluation of hydrogen peroxide sensitive prodrugs of methotrexate and Aminopterin for the treatment of rheumatoid arthritis, J. Med. Chem. 61 (2018) 3503–3515, https://doi.org/10.1021/acs.jmedchem.7b01775.

[4] G.R. Burmester, J.E. Pope, Novel treatment strategies in rheumatoid arthritis, Lancet 389 (2017) 2338–2348, https://doi.org/10.1016/S0140-6736(17)31491-5.

[5] I.B. McInnes, G. Schett, Cytokines in the pathogenesis of rheumatoid arthritis, Nat. Rev. Immunol. 7 (2007) 429–442, https://doi.org/10.1038/nri2094.

[6] A. Marrelli, P. Cipriani, V. Liakouli, F. Carubbi, C. Perricone, R. Perricone, R. Giacomelli, Angiogenesis in rheumatoid arthritis: a disease specific process or a common response to chronic inflammation? Autoimmun. Rev. 10 (2011) 595–598, https://doi.org/10.1016/j.autrev.2011.04.020.

[7] C.T. Pham, Nanotherapeutic approaches for the treatment of rheumatoid arthritis, Wiley. Interdiscip. Rev. Nanomed. Nanobiotechnol. 3 (2011) 607–619, https://doi.org/10.1002/wnan.157.

[8] K. Oda, M. Minata, Drug free remission after steroid-dependent disappearance of lymphoproliferative disorder in rheumatoid arthritis patient treated with TNF-alpha blockade: case study, SpringerPlus 4 (2015) 41, https://doi.org/10.1186/s40064-015-0798-9.

[9] I. Ohsawa, M. Ishikawa, K. Takahashi, M. Watanabe, K. Nishimaki, K. Yamagata, K. Katsura, Y. Katayama, S. Asoh, S. Ohta, Hydrogen acts as a therapeutic antioxidant by selectively reducing cytotoxic oxygen radicals, Nat. Med. 13 (2007) 688–694, https://doi.org/10.1038/nm1577.

[10] K. Fukuda, S. Asoh, M. Ishikawa, Y. Yamamoto, I. Ohsawa, S. Ohta, Inhalation of hydrogen gas suppresses hepatic injury caused by ischemia/reperfusion through reducing oxidative stress, Biochem. Biophys. Res. Commun. 361 (3) (2007) 670–674, https://doi.org/10.1016/j.bbrc.2007.07.088.

[11] H. Liu, R. Colavitti, I.I. Rovira, T. Finkel, Redox-dependent transcriptional regulation, Circ. Res. 97 (2005) 967–974, https://doi.org/10.1161/01.RES.0000188210.72062.10.

[12] H. Sauer, M. Wartenberg, J. Hescheler, Reactive oxygen species as intracellular messengers during cell growth and differentiation, Cell. Physiol. Biochem. 11 (2001) 173–186, https://doi.org/10.1159/000047804.

[13] I. Ohsawa, M. Ishikawa, K. Takahashi, M. Watanabe, K. Nishimaki, K. Yamagata, K. Katsura, Y. Katayama, S. Asoh, S. Ohta, Hydrogen acts as a therapeutic antioxidant by selectively reducing cytotoxic oxygen radicals, Nat. Med. 13 (2007) 688–694, https://doi.org/10.1038/nm1577.

[14] K.M. Kang, Y.N. Kang, I.B. Choi, Y. Gu, T. Kawamura, Y. Toyoda, A. Nakao, Effects of drinking hydrogen-rich water on the quality of life of patients treated with radiotherapy for liver tumors, Med. Gas Res. 1 (2011) 11, https://doi.org/10.1186/2045-9912-1-11.

[15] K. Imai, T. Kotani, H. Tsuda, Y. Mano, T. Nakano, T. Ushida, H. Li, R. Miki, S. Sumigama, A. Iwase, A. Hirakawa, K. Ohno, S. Toyokuni, H. Takeuchi, T. Mizuno, A. Suzumura, F. Kikkawa, Neuroprotective potential of molecular hydrogen against perinatal brain injury via suppression of activated microglia, Free, Radic. Biol. Med. 91 (2016) 154–163, https://doi.org/10.1016/j.freeradbiomed.2015.12.015.

[16] L. Qian, F. Cao, J. Cui, Y. Huang, X. Zhou, S. Liu, J. Cai, Radioprotective effect of hydrogen in cultured cells and mice, Free. Radic. Res. 44 (2010) 275–282, https://doi.org/10.3109/10715760903468758.

[17] Y. Chuai, L. Zhao, J. Ni, D. Sun, J. Cui, B. Li, L. Qian, F. Gao, J. Cai, A possible prevention strategy of radiation pneumonitis: combine radiotherapy with aerosol inhalation of hydrogen-rich solution, Med. Sci. Mon. Int. Med. J. Exp. Clin. Res. 17 (2011), https://doi.org/10.12659/msm.881698. HY1-HY4.

[18] N. Nakashima-Kamimura, T. Mori, I. Ohsawa, S. Asoh, S. Ohta, Molecular hydrogen alleviates nephrotoxicity induced by an anti-cancer drug cisplatin without compromising anti-tumor activity in mice, Cancer Chemother. Pharmacol. 64 (2009) 753–761, https://doi.org/10.1007/s00280-008-0924-2.

[19] P. Zhao, Z. Jin, Q. Chen, T. Yang, D. Chen, J. Meng, X. Lu, Z. Gu, Q. He, Local generation of hydrogen for enhanced photothermal therapy, Nat. Commun. 9 (2018) 4241, https://doi.org/10.1038/s41467-018-06630-2.

[20] J. Li, C. Wang, J.H. Zhang, J.M. Cai, Y.P. Cao, X.J. Sun, Hydrogen-rich saline improves memory function in a rat model of amyloid-beta-induced Alzheimer's disease by reduction of oxidative stress, Brain Res. 1328 (2010) 152–161, https://doi.org/10.1016/j.brainres.2010.02.046.

[21] Y. Fu, M. Ito, Y. Fujita, M. Ito, M. Ichihara, A. Masuda, Y. Suzuki, S. Maesawa, Y. Kajita, M. Hirayama, I. Ohsawa, S. Ohta, K. Ohno, Molecular hydrogen is protective against 6-hydroxydopamine-induced nigrostriatal degeneration in a rat model of Parkinson's disease, Neurosci. Lett. 453 (2009) 81–85, https://doi.org/10.1016/j.neulet.2009.02.016.

[22] J.D. Ren, X.B. Wu, R. Jiang, D.P. Hao, Y. Liu, Molecular hydrogen inhibits lipopolysaccharide-triggered NLRP3 inflammasome activation in macrophages by targeting the mitochondrial reactive oxygen species, Biochim. Biophys. Acta 1863 (2016) 50–55, https://doi.org/10.1016/j.bbamcr.2015.10.012.

[23] T. Ishibashi, B. Sato, M. Rikitake, T. Seo, R. Kurokawa, Y. Hara, Y. Naritomi, H. Hara, T. Nagao, Consumption of water containing a high concentration of molecular hydrogen reduces oxidative stress and disease activity in patients with rheumatoid arthritis: an open-label pilot study, Med. Gas Res. 2 (2012) 27, https://doi.org/10.1186/2045-9912-2-27.

[24] H. Ono, Y. Nishijima, N. Adachi, M. Sakamoto, Y. Kudo, J. Nakazawa, K. Kaneko, A. Nakao, Hydrogen(H2) treatment for acute erythymatous skin diseases. A report of 4 patients with safety data and a non-controlled feasibility study with H2 concentration measurement on two volunteers, Med. Gas Res. 2 (2012) 14, https://doi.org/10.1186/2045-9912-2-14.

[25] B.M. Buchholz, D.J. Kaczorowski, R. Sugimoto, R. Yang, Y. Wang, T.R. Billiar, K.R. McCurry, A.J. Bauer, A. Nakao, Hydrogen inhalation ameliorates oxidative stress in transplantation induced intestinal graft injury, Am. J. Transplant. 8 (2008) 2015–2024, https://doi.org/10.1111/j.1600-6143.2008.02359.x.

[26] J. Hwang, K. Rodgers, J.C. Oliver, T. Schluep, Alpha-methylprednisolone conjugated cyclodextrin polymer-based nanoparticles for rheumatoid arthritis therapy, Int. J. Nanomed. 3 (2008) 359–371, https://doi.org/10.2147/ijn.s3217.

[27] T. Barnes, R. Moots, Targeting nanomedicines in the treatment of rheumatoid arthritis: focus on certolizumab pegol, Int. J. Nanomed. 2 (2007) 3–7, https://doi.org/10.2147/nano.2007.2.1.3.

[28] S. Parveen, R. Misra, S.K. Sahoo, Nanoparticles: a boon to drug delivery, therapeutics, diagnostics and imaging, Nanomedicine 8 (2012) 147–166, https://doi.org/10.1016/j.nano.2011.05.016.

[29] D. Wang, H. Dong, M. Li, Y. Cao, F. Yang, K. Zhang, W. Dai, C. Wang, X. Zhang, Erythrocyte-Cancer hybrid membrane camouflaged hollow copper sulfide nanoparticles for prolonged circulation life and homotypic-targeting photothermal/chemotherapy of melanoma, ACS Nano 12 (2018) 5241–5252, https://doi.org/10.1021/acsnano.7b08355.

[30] R.I. Scheinman, R. Trivedi, S. Vermillion, U.B. Kompella, Functionalized STAT1 siRNA nanoparticles regress rheumatoid arthritis in a mouse model, Nanomedicine 6 (2011) 1669–1682, https://doi.org/10.2217/nnm.11.90.

[35] T. Zhou, Y. Du, A. Borgna, J. Hong, Y. Wang, J. Han, W. Zhang, R. Xu, Post-synthesis modification of a metal–organic framework to construct a bifunctional photocatalyst for hydrogen production, Energy, Environ. Sci. 6 (2013) 3229–3234, https://doi.org/10.1039/C3EE41548A.

[36] Y. Kataoka, H. Sato, Y. Miyazaki, K. Masuda, H. Tanaka, S. Naito, W. Mori, Photocatalytic hydrogen production from water using porous material [Ru2(p-BDC)2]n, Energy, Environ. Sci. 2 (2009) 397–400, https://doi.org/10.1039/b814539c.

[37] Y. Fu, D. Sun, Y. Chen, R. Huang, Z. Ding, X. Fu, Z. Li, An amine-functionalized titanium metal-organic framework photocatalyst with visible-light-induced activity for CO2 reduction, Angew. Chem., Int. Ed. Engl. 51 (2012) 3364–3367, https://doi.org/10.1002/anie.201108357.

[38] K.G. Laurier, F. Vermoortele, R. Ameloot, D.E. De Vos, J. Hofkens, M.B. Roeffaers, Iron(III)-based metal-organic frameworks as visible light photocatalysts, J. Am. Chem. Soc. 135 (2013) 14488–14491, https://doi.org/10.1021/ja405086e.

[39] J.D. Xiao, Q. Shang, Y. Xiong, Q. Zhang, Y. Luo, S.H. Yu, H.L. Jiang, Boosting photocatalytic hydrogen production of a metal-organic framework decorated with platinum nanoparticles: the platinum location matters, Angew. Chem., Int. Ed. Engl. 55 (2016) 9389–9393, https://doi.org/10.1002/anie.201603990.

[40] S. Linic, P. Christopher, D.B. Ingram, Plasmonic-metal nanostructures for efficient conversion of solar to chemical energy, Nat. Mater. 10 (2011) 911–921, https://doi.org/10.1038/nmat3151.

[41] C. Wang, D. Astruc, Nanogold plasmonic photocatalysis for organic synthesis and clean energy conversion, Chem. Soc. Rev. 43 (2014) 7188–7216, https://doi.org/10.1039/c4cs00145a.

[42] M.W. Knight, H. Sobhani, P. Nordlander, N.J. Halas, Photodetection with active optical antennas, Science 332 (2011) 702–704, https://doi.org/10.1126/science.1203056.

[43] L.M. Liz-Marzán, C.J. Murphy, J. Wang, Nanoplasmonics, Chem. Soc. Rev. 43 (2014) 3820–3822, https://doi.org/10.1039/c4cs90026j.

[44] C.H. Hendon, D. Tiana, M. Fontecave, C. Sanchez, L. D'arras, C. Sassoye, L. Rozes, C. Mellot-Draznieks, A. Walsh, Engineering the optical response of the titanium-MIL-125 metal-organic framework through ligand functionalization, J. Am. Chem. Soc. 135 (2013) 10942–10945, https://doi.org/10.1021/ja405350u.

[45] B. Wu, D. Liu, S. Mubeen, T.T. Chuong, M. Moskovits, G.D. Stucky, Anisotropic growth of TiO2 onto gold nanorods for plasmon-enhanced hydrogen production from water reduction, J. Am. Chem. Soc. 138 (2016) 1114–1117, https://doi.org/10.1021/jacs.5b11341.

[46] J. Xiao, L. Han, J. Luo, S. Yu, H. Jiang, Integration of plasmonic effects and Schottky junctions into metal-organic framework composites: steering charge flow for enhanced visible-light photocatalysis, Angew. Chem., Int. Ed. Engl. 57 (2018) 1103–1107, https://doi.org/10.1002/anie.201711725.

[47] M. Bernardi, J. Mustafa, J.B. Neaton, S.G. Louie, Theory and computation of hot carriers generated by surface plasmon polaritons in noble metals, Nat. Commun. 6 (2015) 7044, https://doi.org/10.1038/ncomms8044.

[48] D.W. Wang, S.R. Goldring, The bone, the joints and the Balm of Gilead, Mol. Pharm. 8 (2011) 991–993, https://doi.org/10.1021/mp200328t.

[49] H. Liu, L. Chang, L. Chen, Y. Li, In situ one-step synthesis of metal–organic framework encapsulated naked Pt nanoparticles without additional reductants, J. Mater. Chem. 3 (2015) 8028, https://doi.org/10.1039/c5ta00030k.

[50] Y. Liu, Z. Tang, Multifunctional nanoparticle@MOF core-shell nanostructures, Adv. Mater. 25 (2013) 5819–5825, https://doi.org/10.1002/adma.201302781.

[51] X. Ye, L. Jin, H. Caglayan, J. Chen, G. Xing, C. Zheng, V. Doan-Nguyen, Y. Kang, N. Engheta, C.R. Kagan, C.B. Murray, Improved size-tunable synthesis of monodisperse gold nanorods through the use of aromatic additives, ACS Nano 6 (2012) 2804–2817, https://doi.org/10.1021/nn300315j.

[52] M. Qiu, D. Wang, W. Liang, L. Liu, Y. Zhang, X. Chen, D.K. Sang, C. Xing, Z. Li, B. Dong, F. Xing, D. Fan, S. Bao, H. Zhang, Y. Cao, Novel concept of the smart NIR-light-controlled drug release of black phosphorus nanostructure for cancer therapy, Proc. Natl. Acad. Sci. U. S. A 115 (2018) 501–506, https://doi.org/10.1073/pnas.1714421115.

[53] S.M. Lee, H.J. Kim, Y.J. Ha, Y.N. Park, S.K. Lee, Y.B. Park, K.H. Yoo, Targeted chemo-photothermal treatments of rheumatoid arthritis using gold half-shell multifunctional nanoparticles, ACS Nano 7 (2013) 50–57, https://doi.org/10.1021/nn301215q.

[54] N. Tanaka, H. Sakahashi, K. Hirose, T. Ishima, S. Ishii, Arthroscopic and open synovectomy of the elbow in rheumatoid arthritis, J. Bone Joint Surg. Am. 88 (2006) 521–525, https://doi.org/10.2106/JBJS.E.00472.

[55] H. Liu, L. Chang, C. Bai, L. Chen, R. Luque, Y. Li, Controllable encapsulation of "clean" metal clusters within MOFs through kinetic modulation: towards advanced heterogeneous nanocatalysts, Angew. Chem., Int. Ed. Engl. 55 (2016) 5019–5023, https://doi.org/10.1002/anie.201511009.

[56] D.K. Roper, W. Ahn, M.P. Hoepfner, Microscale heat transfer transduced by surface plasmon resonant gold nanoparticles, J. Phys. Chem. C Nanomater. Interfaces. 111 (2007) 3636–3641, https://doi.org/10.1021/jp064341w.

[57] I. Ohsawa, K. Nishimaki, C. Yasuda, K. Kamino, S. Ohta, Deficiency in a mitochondrial aldehyde dehydrogenase increases vulnerability to oxidative stress in PC12 cells, J. Neurochem. 84 (2003) 1110–1117, https://doi.org/10.1046/j.1471-4159.2003.01619.x.

Further reading

[31] B. Fang, Z. Xing, D. Sun, Z. Li, W. Zhou, Hollow semiconductor photocatalysts for solar energy conversion, Adv. Powder Mater. (2021), https://doi.org/10.1016/j.apmate.2021.11.008.

[32] Q. Cheng, G. Zhang, Enhanced photocatalytic performance of tungsten-based photocatalysts for degradation of volatile organic compounds: a review, Tungsten 2 (2020) 240–250, https://doi.org/10.1007/s42864-020-00055-5.

[33] Y. Qin, Y. Guo, Z. Liang, Y. Xue, X. Zhang, L. Yang, J. Tian, Au nanorods decorated TiO2 nanobelts with enhanced full solar spectrum photocatalytic antibacterial activity and the sterilization file cabinet application, Chin. Chem. Lett. (2020), https://doi.org/10.1016/j.cclet.2020.10.020.

[34] Z. Liang, X. Meng, Y. Xue, X. Chen, Y. Zhou, X. Zhang, H. Cui, J. Tian, Facile preparation of metallic 1T phase molybdenum selenide as cocatalyst coupled with graphitic carbon nitride for enhanced photocatalytic H2 production, J. Colloid Interface Sci. 598 (2021) 172–180, https://doi.org/10.1016/j.jcis.2021.04.066.